Monthly Notices of the ROYAL ASTRONOMICAL SOCIETY

MNRAS **539,** 3582–3595 (2025) https://doi.org/10.1093/mnras/staf666
Advance Access publication 2025 April 24

Sub-day time-scale X-ray spectral variability of the TeV blazars Mrk 421 and 1ES 1959+650

Susmita Das ★ and Ritaban Chatterjee

School of Astrophysics, Presidency University, 86/1 College Street, Kolkata 700073, West Bengal, India

Accepted 2025 April 22. Received 2025 March 22; in original form 2024 July 19

ABSTRACT

We present X-ray spectra (0.7–20 keV) of two high synchrotron-peaked blazars Mrk 421 and 1ES 1959+650 from simultaneous observations by the SXT and LAXPC instruments onboard *AstroSat* and the *Swift*-XRT during multiple intervals in 2016–2019. The spectra of individual epochs are satisfactorily fitted by the log-parabola model. We carry out time-resolved X-ray spectroscopy using the *AstroSat* data with a time resolution of ∼10 ks at all epochs, and study the temporal evolution of the best-fitting spectral parameters of the log-parabola model. The energy light curves, with duration in the range 0.5–5 days, show intra-day variability and change in brightness states from one epoch to another. We find that the variation of the spectral index (α) at hours to days time-scale has an inverse relation with the energy flux and the peak energy of the spectrum, which indicates a harder-when-brighter trend in the blazars. The variation of curvature (β) does not follow a clear trend with the flux and has an anticorrelation with α. Comparison with spectral variation simulated using a theoretical model of time-variable non-thermal emission from blazar jets shows that radiative cooling and gradual acceleration of emitting particles belonging to an initial simple power-law energy distribution can reproduce most of the variability patterns of the spectral parameters at sub-day time-scales.

Key words: galaxies: active – BL Lacertae objects: individual: Mrk 421, 1ES 1959+650 – galaxies: jets – X-rays: galaxies.

1 INTRODUCTION

An active galactic nucleus (AGN) radiates an enormous amount of energy, which may sometimes exceed the host galaxy luminosity. This huge energy is supplied by the accretion of matter towards the central supermassive black hole and is radiated through different components of the AGN, e.g. accretion disc, emission-line clouds, dusty torus, and the outflow of bipolar jets containing magnetized plasma moving at speed close to that of light. When the axis of the relativistic jet is very close to the observer's line of sight, the AGN is classified as a blazar (Blandford & Rees 1978; Urry & Padovani 1995). It is one of the subclasses of radio-loud AGNs, in which the jet emission, amplified by relativistic beaming, dominates the entire spectral energy distribution (SED), which often extends from radio to γ-rays (e.g. Ghisellini et al. 1993; Giommi et al. 2012). Consequently, we can see dramatic variation of luminosity at minutes-years time-scale (e.g. Abdo et al. 2010; Bonning et al. 2012; Chatterjee et al. 2012; Massaro, Thompson & Ferrara 2015; Marscher 2016; Rajput, Stalin & Rakshit 2020). The broad-band continuum emission of blazars is defined by two humps at lower and higher energy regimes. At low energy, the peak is at IR-optical sometimes extending to UV/X-ray, and the higher energy peak lies at the GeV band.

The origin of the two broad peaks in the SED can be explained by the radiation mechanisms that are responsible for jet emission. In the presence of magnetic field, the relativistic electrons in the jet generate synchrotron emission that dominates the lower energy peak of the SED (Bregman et al. 1981; Urry & Mushotzky 1982; Impey & Neugebauer 1988; Marscher 1998; Ghisellini et al. 2017). On the other hand, the origin of the higher energy emission has two possible scenarios. The jet plasma may be made of electrons, positrons, and protons. In the so-called 'leptonic' model, protons are absent or their contribution to the jet emission is negligible. In that scenario, inverse-Compton (IC) scattering by the electrons contributes to the higher energy emission by the upscattering of lower energy 'seed' photons, which may be the synchrotron photons in the jet itself (Konigl 1981; Maraschi, Ghisellini & Celotti 1992; Sikora, Begelman & Rees 1994; Bloom & Marscher 1996; Mastichiadis & Kirk 1997; Böttcher 2007) or photons external to the jet, e.g. from the dusty torus or the broad-line region (Dermer, Schlickeiser & Mastichiadis 1992; Ghisellini et al. 1998; Błażejowski et al. 2000; Böttcher & Dermer 2010), which are defined as synchrotron self-Compton (SSC) or external Compton (EC) process, respectively. On the other hand, protons contribute significantly to the jet emission in the 'hadronic' model. In that case, relativistic protons in the jet may emit synchrotron radiation, or they may produce secondary particles via their interaction with photons (Mücke & Protheroe 2001; Mücke et al. 2003; Böttcher et al. 2013; Ackermann et al. 2016; Bottacini et al. 2016), which contribute to the γ-ray emission of blazars.

Significant fluctuation of the total flux over a range of time-scales is a characteristic property of blazars and their spectral nature, e.g. the frequency of the peak and shape of the lower and higher energy humps vary along with the total flux. In this

★ E-mail: susmita.rs@presiuniv.ac.in

work, we focus on the X-ray spectral variation of two blazars, namely, Mrk 421 and 1ES 1959+650, at minutes to days time-scales. Both of those blazars are high synchrotron-peaked (HSP), i.e. the lower energy peak of their SED is at the UV-X-ray energy range ($\nu_{sync} > 10^{15}$ Hz; Beckmann et al. 2002; Abdo et al. 2011; Banerjee et al. 2019; MAGIC Collaboration 2020). Therefore, X-ray emission provides information about the highest energy electrons in the jet.

Mrk 421 is the first ever TeV-detected blazar in a nearby galaxy at $z = 0.031$. It was first observed by EGERT and Whipple Observatory in 1992 (Lin et al. 1992; Punch et al. 1992; Piner et al. 1999). Later, the broad-band SED and the underlying physical processes in Mrk 421 have been studied using numerous multiwavelength observations (e.g. Brinkmann et al. 2005; Fossati et al. 2008; Lichti et al. 2008; Horan et al. 2009; Abdo et al. 2011; Albert et al. 2022; Markowitz et al. 2022). The lower energy (synchrotron) peak in the SED of Mrk 421 is at 0.1–10 keV and the higher energy peak is at $\sim$ 50 GeV (Abdo et al. 2011; Banerjee et al. 2019). The spectrum of Mrk 421 at the X-ray energies shows a significant curvature in its shape (Landau et al. 1986; Inoue & Takahara 1996; Sambruna, Maraschi & Urry 1996; Takahashi et al. 1996). The curved spectrum, at different flux states, has been satisfactorily fitted with a log-parabola model (Massaro et al. 2004, 2008; Tanihata et al. 2004; Tramacere, Massaro & Cavaliere 2007; Tramacere et al. 2009; Chen 2014; Kapanadze et al. 2017; Bhatta, Mohorian & Bilinsky 2018; Kapanadze et al. 2020) as well as a broken power-law model (Takahashi et al. 1996; Brinkmann et al. 2001, 2005; Chen 2014). In addition, using BeppoSAX, *Swift*, and *XMM–Newton* observations, Massaro et al. (2004, 2006) showed that the electron energy distribution responsible for the X-ray emission through synchrotron radiation in Mrk 421 approximately follows a log-parabolic function. Massaro et al. (2008) showed that the X-ray spectra of several other HSP blazars are well described by the log-parabola model and exhibit significant correlation between certain spectral parameters, which is consistent with the statistical/stochastic acceleration process in the jet. The curvature of the X-ray spectrum is also well described by certain physically motivated models of energy-dependent particle distributions, e.g. energy-dependent diffusion (EDD), energy-dependent acceleration (EDA), and power law with a high-energy cut-off (Goswami et al. 2018, 2020; Hota et al. 2021; Khatoon et al. 2022).

1ES 1959+650 ($z = 0.048$) is one of the first blazars detected at TeV energies by the Utah Seven Telescope Array experiment (Nishiyama 1999). It was studied at X-ray energies for the first time by the Einstein-IPC in 1992 (Elvis et al. 1992), and later by ROSAT in 1996, BeppoSAX in 1997, and by Rossi X-Ray Timing Explorer (RXTE) in 2000 (Beckmann et al. 2002; Giebels et al. 2002). The broad-band SED has been studied by many authors (e.g. Böttcher & Dermer 2010; Aliu et al. 2013; Kapanadze et al. 2016; MAGIC Collaboration 2020; Chandra et al. 2021) and it is found that both leptonic and hadronic models may be used to fit the SED satisfactorily. At the X-ray band, the spectrum is curved and is fit better by the log-parabola function compared to other models (Tagliaferri et al. 2003; Tramacere et al. 2009; Kapanadze et al. 2018; Chandra et al. 2021; Wani, Gaur & Patil 2023). From X-ray spectral fitting, it is possible to probe relations, if any, between the best-fitting model parameters, which may provide physical information regarding the emission processes involved. In Shah et al. (2021), the X-ray spectrum is described by synchrotron radiation generated by different particle energy distributions, e.g. log-parabola and broken power law, with the latter providing a better fit. They have shown that the particle number density is anticorrelated with the best-fitting power-law index below the break energy, which depicts a connection of acceleration and cooling mechanisms of the particles in the emission region.

Polarization at multiple wave bands provides information, which are complimentary to that obtained from variability and spectroscopy. Hence, it is an effective probe of the physical processes in jets. In the last two years, Imaging X-ray Polarimetry Explorer (IXPE) is carrying out X-ray polarization observations of blazars with unprecedented details (Weisskopf et al. 2022). Strong X-ray polarization ($\sim$10–20 per cent) has been detected in several HSP blazars, including those in our sample, e.g. Mrk 421 and 1ES 1959+650, while in low synchrotron-peaked (LSP) blazars IXPE observations have mostly come up with only upper limits but no detection (e.g. Liodakis et al. 2022; Di Gesu et al. 2023; Middei et al. 2023). That has provided support to the notion that X-rays generated in the synchrotron process are strongly polarized, while it is weak in X-rays produced by the IC process, latter being the case in LSP blazars. In the hadronic scenario, X-rays in LSP blazars may be due to proton synchrotron process and expected to be strongly polarized. Therefore, non-detection of polarization in those sources indicates that the hadronic process does not contribute significantly to the X-ray emission in those blazars (Peirson & Romani 2018, 2019; Errando et al. 2024; Kim et al. 2024). The detected X-ray polarization fraction in the above HSP blazars is $\sim$1.5–3 times higher than that at the optical and longer wavelengths. That is consistent with the energy stratification of blazar jets, i.e. highest energy particles, such as those emitting X-rays in HSP blazars, remain confined to a small region, e.g. behind a moving shock front that is causing the energization of the emitting particles, while lower energy particles, emitting at longer wavelengths, are located in a larger region. Magnetic field in the smaller region containing X-ray-emitting particles is stronger and more aligned giving rise to higher polarization fraction (Liodakis et al. 2022; Kouch et al. 2024; Marscher et al. 2024).

The two blazars in our sample have been observed with *AstroSat* at several epochs during 2016–2019 giving rise to X-ray light curves and spectra at minutes to days as well as $\sim$months time-scales. The temporal variability of the soft and hard X-ray flux of the two blazars, during those epochs, was analysed and interpreted in a previous work (Das & Chatterjee 2023). They found that the hard and soft X-ray variability are strongly correlated and the time lag is zero in the majority of the epochs although significant hard and soft lags were also present in a few cases. Here, we aim to find the best-fitting model of the X-ray spectra during those epochs and whether they tend to fluctuate from one epoch to another. We further study the time-resolved spectra to study the variability at sub-day time-scales and find correlation between the best-fitting spectral parameters. We explore the possible physical explanation of the observed correlation trends. For that purpose, we compare the results with those of a theoretical model consisting of a multizone emission region, in which initially quiescent electrons are energized by a moving shock front. The electron energy distribution and magnetic field in different cells in the emission region are independent of each other and the former evolves with time due to emission of non-thermal radiation. Such an emission scenario in blazar jets is consistent with various observations, including those by IXPE as discussed above. The time-resolved spectra obtained from the above model and the correlation of the best-fitting model parameters may be compared with the observed results obtained from analysing the *AstroSat* data in order to test the said emission scenario and to constrain the geometry and emission parameters in the jets of those blazars.

In Section 2, we describe the data reduction process to generate the X-ray spectra from *AstroSat* and *Swift* observations. In Section 3,

Table 1. Best-fitting parameter values from log-parabola modelling of XRT+SXT +LAXPC spectra.

Source	Epoch	Constant[a]	α	β	E_{peak} (keV)	$\log_{10}$Flux in CGS (0.7–20 keV)	χ^2/dof
1ES 1959+650	2016 Nov 3–7	0.77 ± 0.02	1.99 ± 0.01	0.35 ± 0.02	0.98 ± 0.05	-9.42 ± 0.15	1.07
	2016 Nov 16	0.81 ± 0.03	1.97 ± 0.03	0.42 ± 0.03	1.09 ± 0.09	-9.34 ± 0.006	1.03
	2017 Oct 25–26	0.77 ± 0.01	1.72 ± 0.01	0.32 ± 0.01	2.69 ± 0.07	-8.92 ± 0.12	1.17
Mrk 421	2017 Jan 3–8	0.71 ± 0.01	1.81 ± 0.01	0.26 ± 0.02	2.25 ± 0.05	-8.92 ± 0.08	1.4
	2017 Jan 24	0.71 ± 0.02	1.97 ± 0.02	0.33 ± 0.02	1.07 ± 0.07	-9.12 ± 0.01	1.11
	2017 Nov 19	0.77 ± 0.02	1.91 ± 0.02	0.37 ± 0.02	1.30 ± 0.08	-9.00 ± 0.003	0.95
	2018 Jan 19–20	0.75 ± 0.01	2.02 ± 0.01	0.31 ± 0.01	0.91 ± 0.05	-8.89 ± 0.02	1.38
	2019 Apr 23–28	0.69 ± 0.01	1.94 ± 0.01	0.12 ± 0.01	1.78 ± 0.12	-8.97 ± 0.04	1.44

Note. [a]Constant is the flux normalization factor of LAXPC corresponding to SXT.

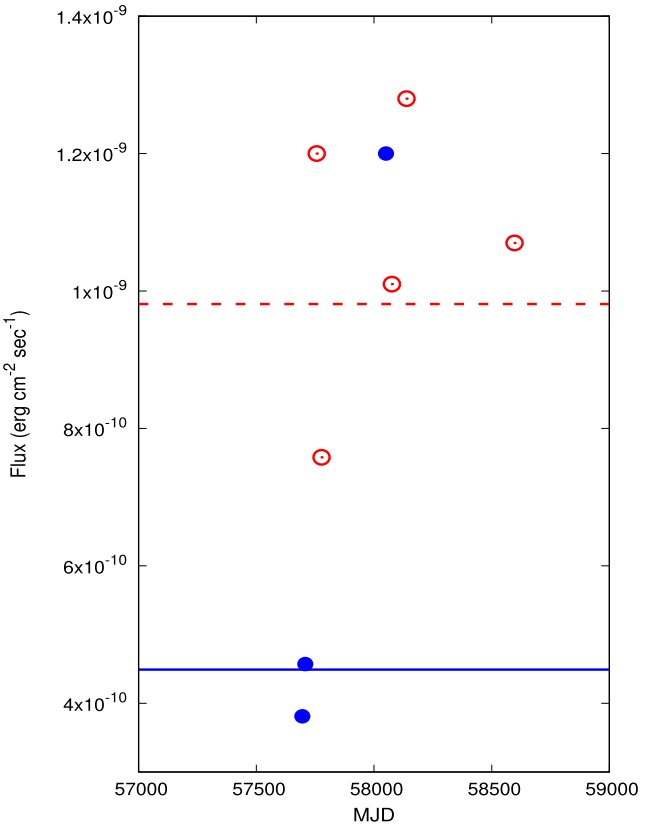

Figure 1. Brightness state of Mrk 421 (red) and 1ES 1959+650 (blue) where the circles denote the epochs of *AstroSat* observations and the lines are average-monitored flux from *Swift*-XRT during 2013–2023.

we analyse the 0.7–20 keV spectrum for each epoch and perform time-resolved spectroscopy in bins of a few hours to study spectral variation with time. In Section 4, we discuss our results and present a theoretical model of non-thermal emission from blazar jets, and use it to interpret the spectral variability at hours to days time-scales. Finally, in Section 5, we summarize our findings.

2 DATA

The X-ray data of the blazars Mrk 421 and 1ES 1959+650 used in this work are from *AstroSat* and the *Neil Gehrels Swift Observatory*. We use data from the instruments named Soft X-ray Telescope (SXT; Singh et al. 2014, 2016, 2017) and Large Area X-ray Proportional Counter (LAXPC; Yadav et al. 2016; Antia et al. 2017) of *AstroSat* and X-Ray Telescope (XRT) of *Swift*, working in the energy range 0.3–8, 3–80, and 0.3–10 keV, respectively. These observed data sets are available in the respective repositories.[1,2] The data consist of three epochs for 1ES 1959+650 and five for Mrk 421 during 2016–2019 as given in Table 1. Preliminary reduction and analyses of SXT and LAXPC data, and details of the final data sets are described in Das & Chatterjee (2023).

We have collected *Swift*-XRT data, the duration of which overlaps with *AstroSat* observations during 2016–2019. We get a total of eight observations of Mrk 421 and four observations of 1ES 1959+650 of duration ∼1 ks in Windowed Timing mode. The light curves and spectra of the source at 0.3–10 keV energy range are generated by the *Swift*-XRT data products building tool[3], which uses HEASOFT version 6.29 (Evans et al. 2009). Fig. 1 exhibits the brightness levels of the two blazars during the epochs used here compared to their respective average flux during 2013–2023 using *Swift*-XRT data.

We note that X-ray-bright HSP blazars, such as the two in our sample, have been observed multiple times by several X-ray telescopes, and their spectra have been analysed and interpreted in detail. However, *AstroSat* has observed the blazars Mrk 421 and 1ES 1959+650 several times within a short span of a few years. Individual observations are able to provide data points with sufficient S/N ratio even when binned to 10-min intervals in some cases (Das & Chatterjee 2023), while multiple epochs of observations provide variability information at months-years time-scales. Such detailed flux and spectral variability information at a broad (0.7–20 keV) energy range is not easily available even for bright HSP blazars like the above two. Therefore, the data set used here is uniquely comprehensive.

3 RESULTS

3.1 X-ray spectral analyses

We carry out the spectral analysis using XSPEC (version 12.10), a tool of HEASOFT. The command GRPPHA helps to group the source spectrum with response and background files. The energy channels are grouped here by a minimum of 30 counts per bin. We analyse SXT and LAXPC spectra jointly in the energy range 0.7–20 keV by loading the spectra in XSPEC. Below 0.7 keV, there are certain

[1]https://astrobrowse.issdc.gov.in/astro_archive/archive/Home.jsp
[2]https://heasarc.gsfc.nasa.gov/
[3]https://www.swift.ac.uk/user_objects/index.php

instrumental artefacts in the SXT spectra, while the background, in LAXPC, starts to dominate at energies higher than 20 keV (Hota et al. 2021; Shah et al. 2021). Thus, we ignore those energy ranges to carry out our analyses. The spectral data from *Swift*-XRT during the epochs 2017 January 3 and 2019 April 23 for Mrk 421, and 2016 November 3 and 2017 October 25 for 1ES 1959+650 at 0.7–7 keV range are used because those epochs overlap with that of the *AstroSat* observations.

The combined spectra are fitted using an empirical model, namely, log-parabola in XSPEC. There is a flux normalization offset between different instruments, which is represented by a constant factor in the spectral modelling. The Galactic hydrogen column density (n_H) values for the line of sight containing Mrk 421 and 1ES 1959+650 are fixed at 1.92×10^{20} and 1.07×10^{21} cm^{-2} (Kalberla et al. 2005), respectively. We add 3 per cent systematic error and perform the gain correction for SXT spectra (Chandra et al. 2021). The time-averaged spectra are satisfactorily fitted by the log-parabola model. The best-fitting models and data are shown in the appendix. The best-fitting values of the parameters of the model and the reduced χ^2 values are given in Table 1. The average flux varies by a factor of 3–4 between epochs, and the best-fitting values of the spectral parameters fluctuate as well. The peak energy shifts from 0.9 to 2.7 keV for the two sources. The fit statistics for the epochs described here are comparable to those in the case of the broken power-law model (Das & Chatterjee 2023). We used the former model for the following time-resolved spectral analyses because the synchrotron peak of those two blazars are in the 0.7–20 keV energy range and log-parabola function is a more natural choice as the shape of the peak. In addition, it is often used by other authors, making it more useful in comparing our results with those found in the literature.

3.2 Time-resolved spectroscopy

To study the nature of spectral variability at sub-day time-scale, we divide the data of all epochs of the two blazars into time segments of length 10 ks. For each time bin, we generate the SXT spectrum using 'filter time file' in XSELECT[4] and the LAXPC spectrum using the LAXPC software by dividing the good time intervals into the above time bins. The spectra in each bin from SXT and LAXPC are fit together using XSPEC by the log-parabola model within 0.7–20 keV. We estimate the unabsorbed flux values at 0.7–20 keV from the fitted time-resolved spectra and determine the energy flux light curves, which are shown in Fig. 2. The nature of variation exhibited by the energy light curves are similar to that of the photon flux shown in Das & Chatterjee (2023). We obtain the best-fitting values of the spectral model parameters in every time bin of each epoch and then investigate whether there is any inter-relation between the variability of different pairs of parameters. The inter-relations between the derived spectral parameters are shown in Figs 3 and 4. Similar analyses for the *Swift*-XRT spectra of individual observations overlapping with the *AstroSat* epochs have been carried out and are shown in the same figures.

From time-resolved spectroscopy, it is observed that the X-ray spectra of both blazars tend to vary in all of the epochs, i.e. the spectral parameters α, β, and corresponding peak energy (E_{peak}) in the log-parabola model are varying significantly from one time-bin to another. The spectral index is in the range 1.5–2.2 and the curvature range is 0.1–0.7, which is slightly higher than that reported by Massaro et al. (2004) but are consistent with the values obtained by Massaro, Paggi & Cavaliere (2011). The peak energy varies from approximately 0.5 to 4 keV among all epochs. The dependence of parameters on flux values shows that α is decreasing and E_{peak} is increasing with increasing flux for all observations, but there is no clear pattern in the variation of β. On the other hand, α has an inverse relation with $E_{\rm peak}$, while β shows a weak correlation with the same, and α and β have a trend of anticorrelation with each other. We note that among the observed intervals, the above trends are weaker in both sources during the epochs of lower flux. Table 2 shows the strength of correlation and their significance during those of the above epochs, which have durations longer than a day.

[4]https://github.com/scsaao/SXT_std_ProductMaker

4 DISCUSSION

The spectral index (α) and the total observed flux are strongly anticorrelated at most epochs for both blazars. This result, also found by other authors (Kapanadze et al. 2017, 2018; Chandra et al. 2021; Hota et al. 2021; Wani et al. 2023), implies the 'harder-when-brighter' nature found in blazars, i.e. spectral hardening (a decrease in absolute value of α) with increasing flux. In addition, there is anticorrelation between α and peak energy ($E_{\rm peak}$), which is a consequence of a higher value of peak energy when the spectrum is flatter.

In some HSP blazars the spectral curvature (β) and peak energy (E_{peak}) are anticorrelated, which has been explained by energy dependent acceleration probability of emitting electrons (Massaro et al. 2006, 2008). The amount of energy-gain by acceleration (ϵ) is inversely proportional to the curvature ($\beta \propto 1/\log(\epsilon)$) and $E_{peak} \propto \epsilon$. Hence, the inverse trend of β and E_{peak} follows. A similar trend has been observed in Mrk 421 from long-term *Swift* and *XMM–Newton* observations (Tramacere et al. 2007; Tramacere et al. 2009; Kapanadze et al. 2017, 2020). However, in the individual epochs discussed here, the correlations between the variation of β and total flux or E_{peak} are weak and in some epochs the sense changes such that they are weakly correlated or anticorrelated. Therefore, over the longer time-scale encompassing all epochs, there is no correlation between the above quantities.

Hota et al. (2021) have analysed the *AstroSat* data from the 2017 January 3–8 epoch of Mrk 421. They fit the observed spectrum with that emitted by a log-parabolic particle distribution in the synchrotron process. They have shown that the observed flux and curvature are weakly correlated, which is consistent with our findings. Khatoon et al. (2022) have found a similar trend of weak correlation for long-term Mrk 421 observations. The curvature of the spectrum may also be due to efficient stochastic acceleration of emitting electrons by magnetic turbulence at the shock front (Massaro et al. 2011; Kapanadze et al. 2016, 2017) in HSP blazars, if the diffusion coefficient is inversely proportional to the curvature parameter. Hence, the combined effect of statistical and stochastic acceleration process may weaken the correlation results.

Massaro et al. (2006, 2008) have found a positive correlation of the spectral index α with curvature β. Similarly, Kapanadze et al. (2018) have obtained a strong linear relation between those parameters during a flaring event of Mrk 421 in 2016 observed by *Swift*-XRT. Considering statistical acceleration, Massaro et al. (2004) have shown that a positive correlation occurs when the electron distribution is of log-parabola nature under the condition, in which the acceleration probability decreases with increasing particle energy. On the other hand, considering the log-parabolic particle

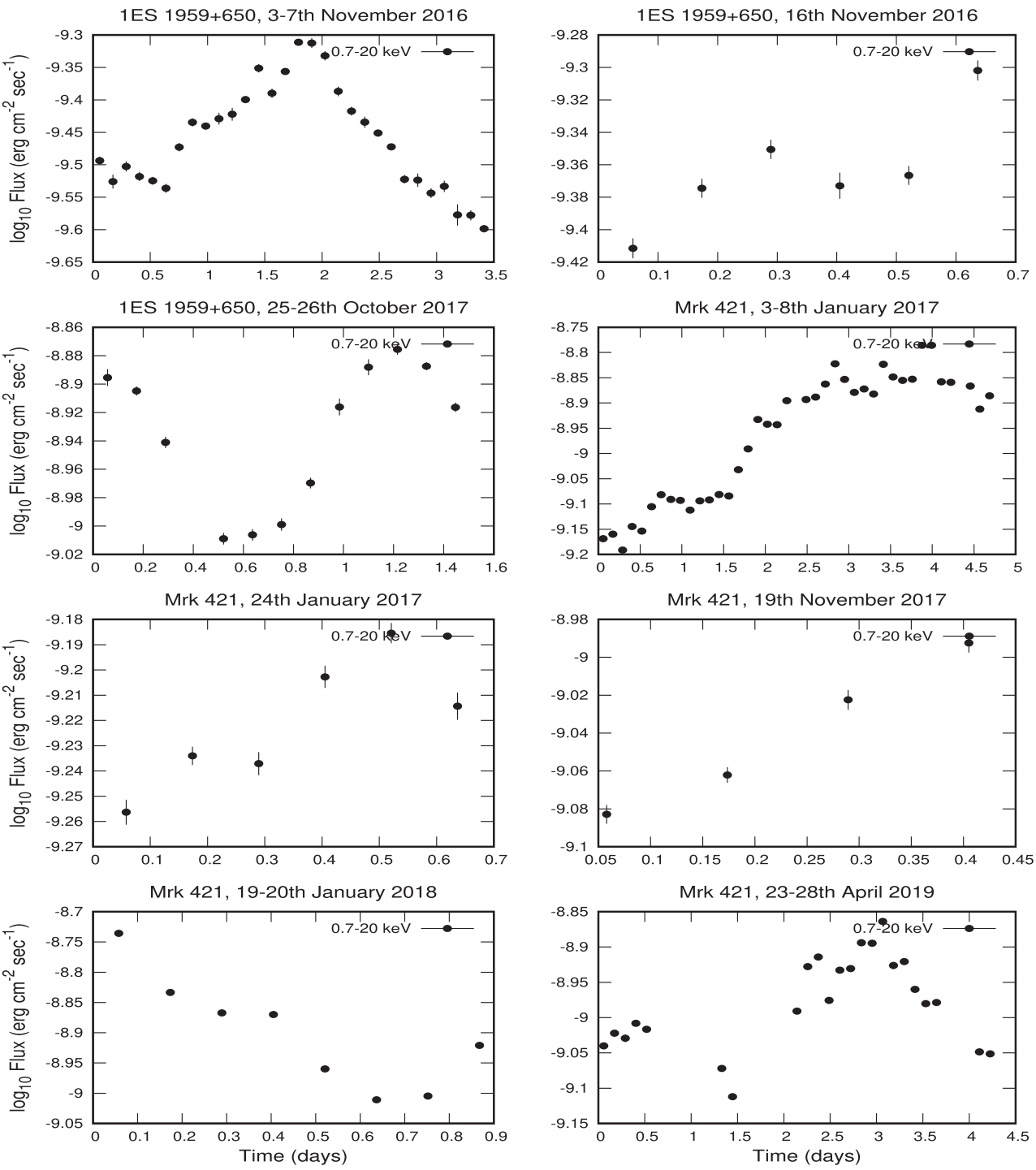

Figure 2. The energy flux light curves of the blazars 1ES 1959+650 and Mrk 421 from time-resolved spectroscopy with 10 ks bins obtained from fitting the *AstroSat* data with log-parabola model at multiple epochs during 2016–2019.

energy distribution, Hota et al. (2021) and Khatoon et al. (2022) have found an opposite nature, i.e. a negative relation between α and β during days and years-long observations of Mrk 421. During the epochs described here, α and β have an anticorrelation. Hence, any clear trend in the α–β relationship, consistently present at epochs separated by ∼years, is absent, which may be caused by different physical mechanisms dominating the spectral variation at different epochs.

The chromatic behaviour of multiwavelength polarization, i.e. stronger polarization at X-ray compared to longer wavelengths in HSP blazars, supports the energy stratification caused by a shock moving down the jet and energizing electrons (Liodakis et al. 2022; Errando et al. 2024; Marscher et al. 2024). However, the direction of X-ray polarization w.r.t. the jet axis and its rotation at days time-scale, as observed by IXPE, are sometimes not consistent with the shock-in-jet model, which indicates

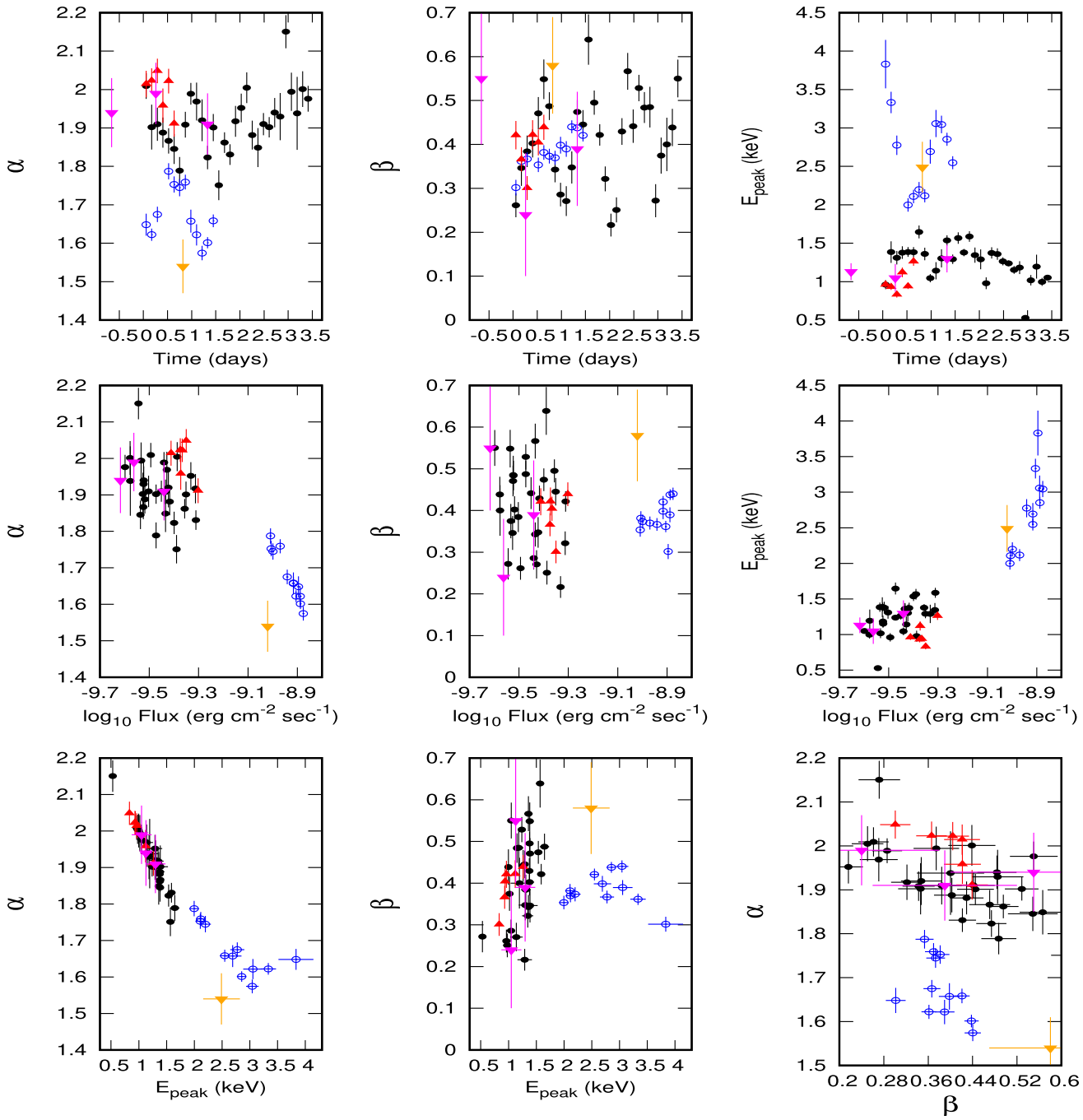

Figure 3. Correlation between best-fitting spectral parameters of the log-parabola model from time-resolved spectroscopy of the *AstroSat* data of the blazar 1ES 1959+650 with time bins of length 10 ks. The black solid circles, red triangles, and blue open circles denote the 2016 November 3, 2016 November 16, and 2017 October 25 epochs, respectively. The inverted triangles (orange and magenta for 2016 November 3 and 2017 October 25 epoch, respectively) denote *Swift*-XRT observations.

the presence of turbulent and/or helical magnetic field structure, as well as the contribution of other dominant processes, e.g. magnetic reconnection or stochastic acceleration (Marscher 2014; Sironi & Spitkovsky 2014; Tavecchio 2021) in the energizaton of the emitting particles. Therefore, examining detailed spectral and timing properties of jet emission, particularly from the highest energy particles, in the context of different theoretical scenarios is important.

Many authors have explored various multizone models of blazar emission containing different geometry and physical structure (Graff et al. 2008; Joshi & Böttcher 2011; Chen 2014; Marscher 2014; Liu et al. 2023; Hu et al. 2024) to understand the temporal and spectral behaviour of jet emission. Different models emphasize certain aspects of jets based on the output intended for further study, e.g. SED, flux variability, polarization. For example, Hota et al. (2021) fit the spectrum of Mrk 421 in the 2017 January 3

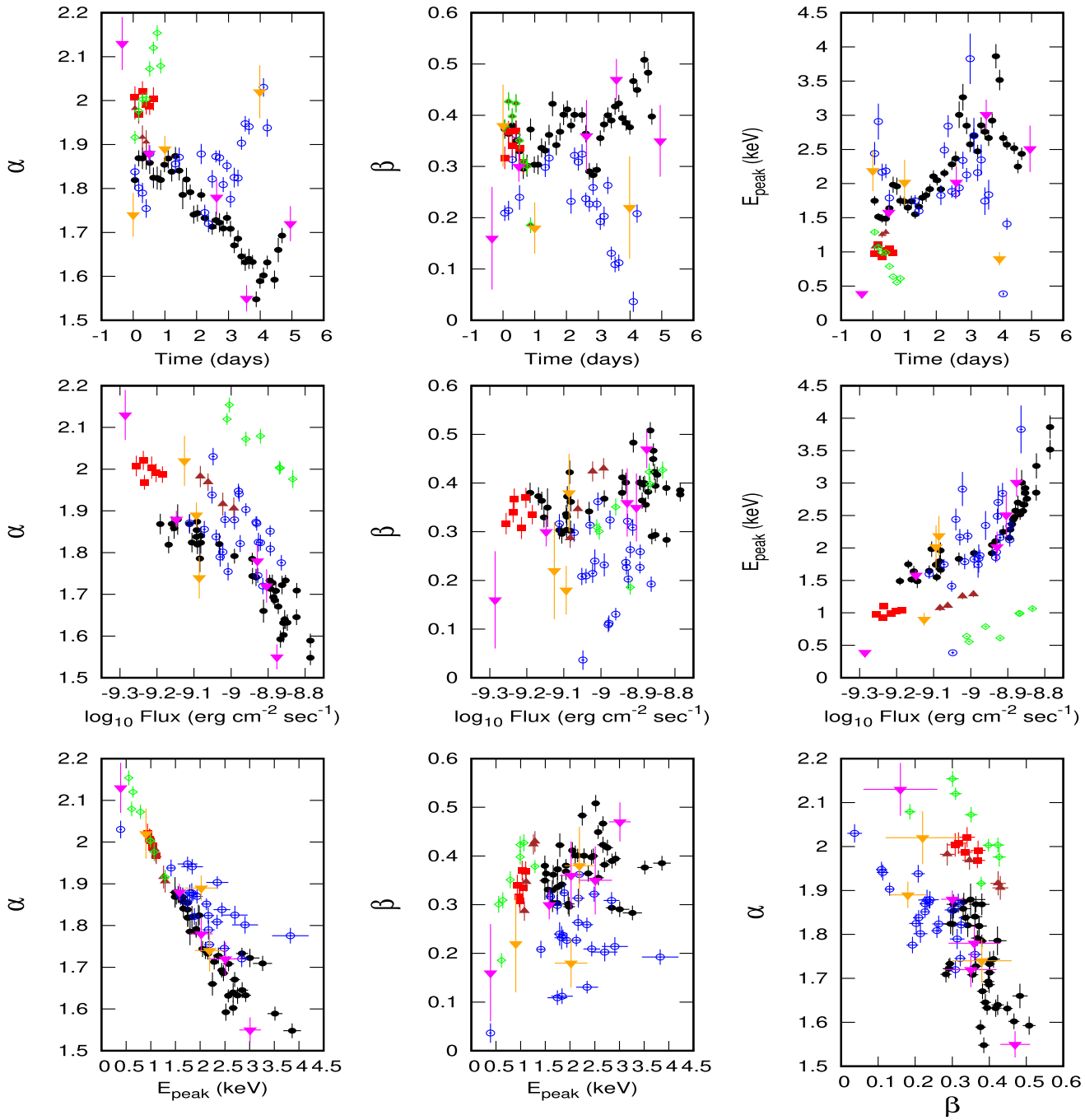

Figure 4. Correlation between best-fitting spectral parameters of the log-parabola model from time-resolved spectroscopy of the *AstroSat* data of the blazar Mrk 421 with time bins of length 10 ks. The black solid circles, red filled squares, maroon triangles, green diamonds, and blue open circles denote the 2017 January 3, 2017 January 24, 2017 November 19, 2018 January 19, and 2019 April 23 epochs, respectively. The inverted triangles (orange and magenta for 2017 January 3 and 2019 April 23 epoch, respectively) denote *Swift*-XRT observations.

epoch with synchrotron radiation emitted by various initial particle distributions, e.g. log-parabolic, power-law with a high-energy cut-off, system having EDD and EDA, etc. and studied the correlation between the best-fitting parameters of the above models. They argued about the suitability of the assumed particle energy distribution models based on the results they obtained. Khatoon et al. (2022) did a similar work for the long-term X-ray variation of the same blazar during 2005–2020. That is an effective approach to probe the underlying emission processes and physical parameters in the jet. Here, we study the spectral variability of two blazars in 10 ks intervals at 3–5 epochs during 2016–2019. We attempt to interpret our observational results in the context of an extensive multizone model, which focuses on the flux and spectral variability at hours-days time-scales. In the theoretical model we use, the acceleration of the electrons may be instantaneous or gradual, the magnetic field structure of the emission region is configurable, and IC process is also included. Although the contribution of the IC emission at the SXT and LAXPC energy bands is negligible for the sources described in

Table 2. Spearman's rank correlation coefficients between the best-fitting parameters from fitting the observed spectra of 1ES 1959+650 and Mrk 421 with the log-parabola model during two epochs, with exposure times of several days, for each of the blazars.

1ES 1959+650	2016 Nov 3–7		2017 Oct 25–26	
	r^a	p^a	r	p
$\alpha - F_{(0.7–20\ \mathrm{keV})}$	− 0.34	0.06	− 0.97	1e-7
$\alpha - E_{\mathrm{peak}}$	− 0.94	5e-15	− 0.84	6e-4
$\beta - F_{(0.7–20\ \mathrm{keV})}$	− 0.15	0.4	0.47	0.12
$\beta - E_{\mathrm{peak}}$	0.44	0.015	0.006	0.98
$E_{\mathrm{peak}} - F_{(0.7–20\ \mathrm{keV})}$	0.34	0.06	0.84	5e-4
$\alpha - \beta$	− 0.64	1e-4	− 0.51	0.09
Mrk 421	**2017 Jan 3–8**		**2019 Apr 23–28**	
	r	p	r	p
$\alpha - F_{(0.7–20keV)}$	− 0.9	3e-15	− 0.41	0.05
$\alpha - E_{peak}$	− 0.9	4e-15	− 0.41	0.05
$\beta - F_{(0.7–20\ \mathrm{keV})}$	0.34	0.03	− 0.016	0.94
$\beta - E_{\mathrm{peak}}$	− 0.27	0.09	0.1	0.62
$E_{\mathrm{peak}} - F_{(0.7–20\ \mathrm{keV})}$	0.95	1e-21	0.58	0.003
$\alpha - \beta$	− 0.6	3e-5	− 0.63	0.001

Note. $^a r$ is the Spearman's correlation coefficient; p denotes the probability that the null hypothesis (the quantities are uncorrelated) is true in the given sample.

Table 3. Fixed parameter values used in the theoretical model of jet emission.

Model parameter	Value
Bulk Lorentz factor (Γ)	15
Doppler factor (δ)	20
Viewing angle with jet axis (θ) in degree	2.7
Slope of electron distribution (s)	2.1
Minimum Lorentz factor of electron (γ_{min})	100
Magnetic field in the first cell (B_i) in G	0.2
Magnetic field in the last cell (B_f) in G	0.1

this work, the energetic electrons in our model cool through both synchrotron and IC processes, which makes the resultant broad-band spectrum closer to observations and hence makes our obtained inferences fairly robust. We describe the model below.

4.1 Jet emission model and its comparison with observed results

In this model, discussed in detail by Barat, Chatterjee & Mitra (2022) and Kundu et al. (2022), a cylindrical emission region is assumed along the jet axis with a fixed viewing angle (θ). The emission region consists of multiple cells of equal size, having individual electron distribution and magnetic field. A shock front moves through the emission region and energizes each cell instantaneously by injection of high-energy electrons. Those electrons then cool through synchrotron and IC processes and give rise to the emission.

In each cell, the initial distribution of electron energy is a power law given by $N(\gamma) = N_0\,\gamma^{-s}$, where γ is the Lorentz factor of electrons with lower and upper limits γ_{min} and γ_{max}, respectively, while s and N_0 are constants. The electron energy evolves as $\mathrm{d}\gamma/\mathrm{d}t = -k_2\gamma^2$ due to radiative cooling. Here, $k_2 = \frac{4\sigma_T}{3m_ec}(U_B + U_R)$, σ_T is the Thomson scattering cross-section, U_B is the magnetic energy density, and U_R is the energy density of seed photons for SSC radiation. To simulate X-ray emission by the synchrotron process as is the case for the two HSP blazars discussed here, we use a set of input parameters for our model, which are listed in Table 3. We simulate light curves at soft (0.7–7 keV) and hard (7–20 keV) X-ray energies of duration ∼5 days, which are corrected for light-travel time effect to reach the observer's frame. We bin the simulated data in intervals of 5 ks. We use shorter time bins compared to those used in the observed data to facilitate the identification of the trends in the variation of the best-fitting spectral parameters and to avoid the influence of spurious changes, if any, in our interpretation. It will also help in comparing those results with other observed data sets, in which use of shorter time bins is possible. Then, we fit the $0.7 - 20$ keV spectrum at each interval with a log-parabola function. Thus, we obtain the temporal variation of the best-fitting parameters similar to what we calculated from the observed data. In Das & Chatterjee (2023), we found both zero and non-zero (hard/soft) time lags between the hard and soft X-ray light curves during the above epochs. The non-zero lags can be explained by gradual acceleration and synchrotron cooling processes. Therefore, in order to generate X-ray light curves with similar temporal properties, we consider two cases, e.g. one in which

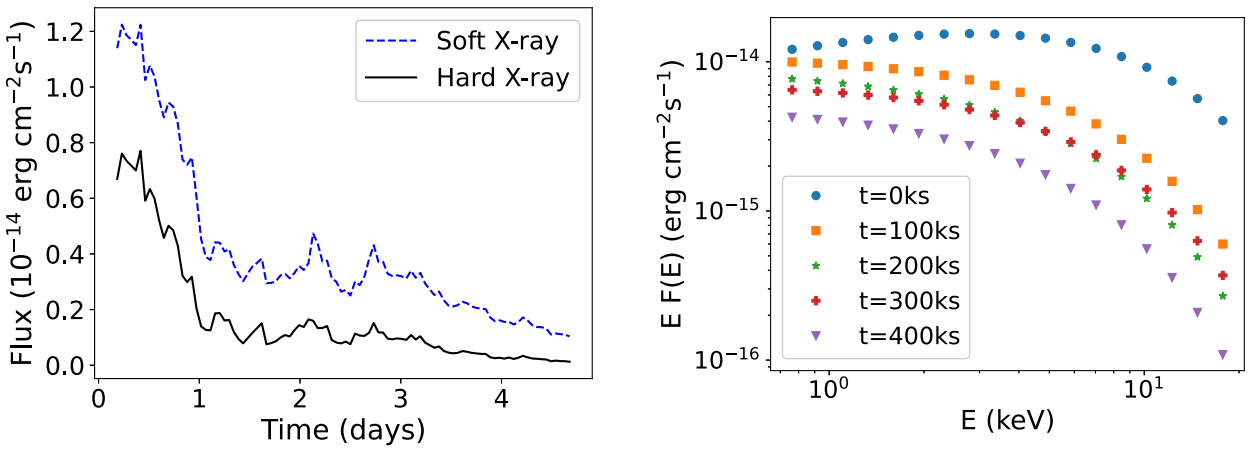

Figure 5. Left panel: soft (0.7–7 keV) and hard X-ray (7–20 keV) light curves simulated using the theoretical model discussed in the text for the case of radiative cooling only. Right panel: evolution of the simulated SED at the X-ray (0.7–20 keV) energy range during a total time interval of ∼5 days (comparable to the longer of the observed light curves in our data).

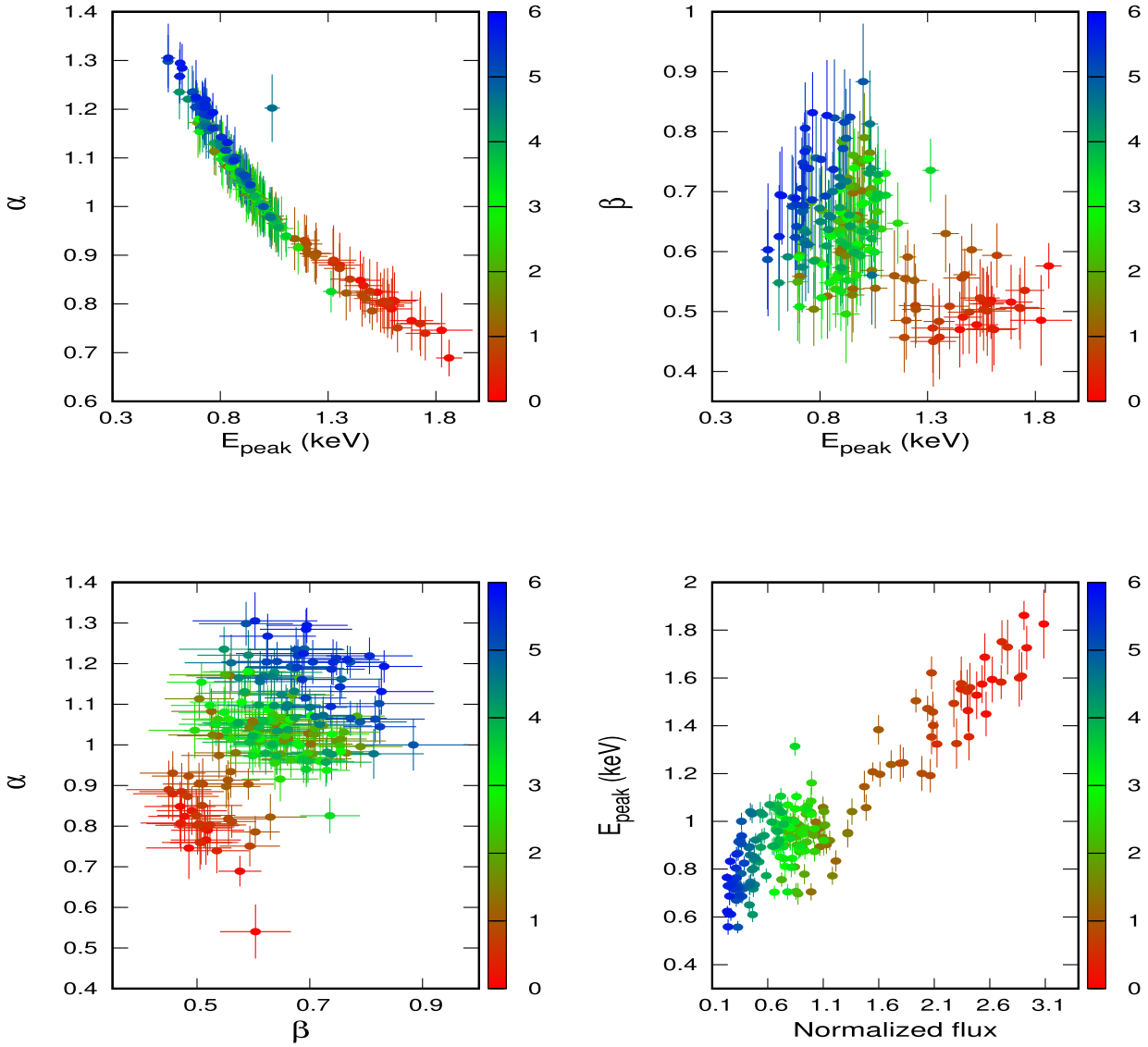

Figure 6. Correlation between the spectral parameters of the log-parabola models, which are best fit to the simulated X-ray spectra at each snapshot of 5 ks duration for the case of radiative cooling only. The colour bar indicates time evolution in days.

the synchrotron cooling time-scale of the highest energy electrons dominates over the acceleration time-scale giving rise to soft lags and another in which the acceleration time-scale dominates causing hard lag. We discuss those two cases below.

4.1.1 Case-I: radiative cooling

When radiative cooling dominates, we fix γ_{max} at a high value (10^5–10^6) in each cell such that the synchrotron peak is at keV energies, as observed in the blazars in our sample. The simulated light curves and spectra are shown in Fig. 5. Fig. 6 shows the correlations between pairs of spectral parameters of the best-fitting log-parabola models at individual time-bins. It shows that α has a strong anticorrelation with the peak energy E_{peak}, which is similar to what we found in the observed data in most epochs. At the beginning, i.e. soon after the energy injection, the peak energy (γ_{max}) of individual cells is high and consequently the power-law index of the emitted spectrum is flatter and the emitted flux is also high. As time passes, the electron energy distribution in the cells becomes steeper (magnitude of s becomes larger) causing the emitted spectrum to become steeper (value of α becomes higher). This happens because higher energy electrons cool faster through synchrotron radiation, e.g. $t_{cool} \sim \gamma^{-1}$, which causes the relative fraction of higher energy electrons to decrease with time. This is accompanied by an overall decrease in the emitted flux because the emitting electrons lose energy through radiative cooling. That causes the α–E_{peak} anticorrelation in the theoretical result such as that exhibited in Fig. 6 top left panel. In the case of β versus E_{peak}, the simulated data show correlation in some sub-intervals, denoted by different colours in Fig. 6 top right panel. However, the overall trend considering the entire time span (∼5 days) of the simulation is of weak anticorrelation. Consequently, the variation of α and β exhibits weak anticorrelation in some sub-intervals, while there is a weak correlation over the total time span, as shown in Fig. 6 bottom left panel. On the other hand, the flux and peak energy are correlated in the simulation as shown in Fig. 6 bottom right panel, which is consistent with the observed harder-when-brighter trend.

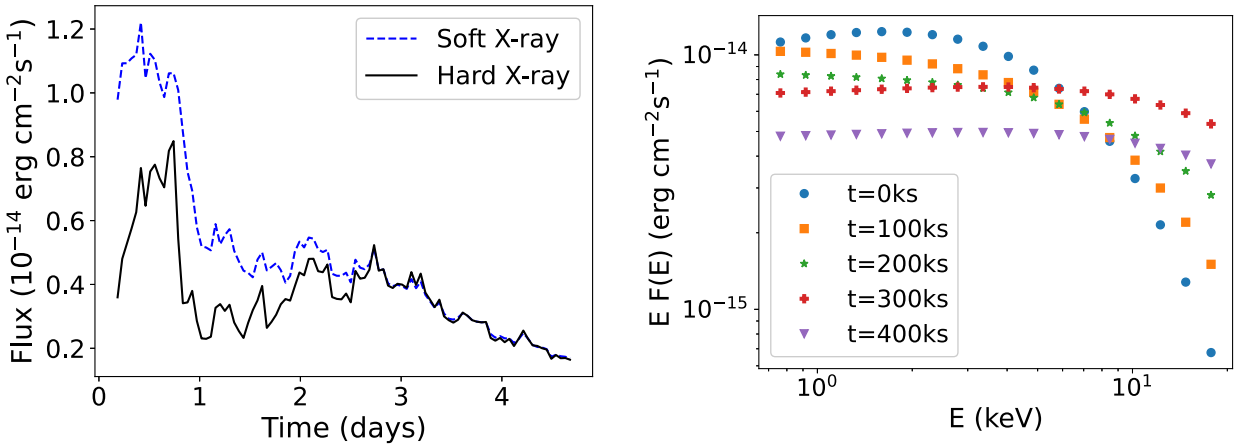

Figure 7. Left panel: soft (0.7–7 keV) and hard X-ray (7–20 keV) light curves simulated using the theoretical model discussed in the text for the case of gradual acceleration. Right panel: evolution of the simulated SED at the X-ray (0.7–20 keV) energy range during a total time interval ∼ 5 days (comparable to the longer of the observed light curves in our data).

4.1.2 Case-II: gradual acceleration and radiative cooling

In this case, we implement gradual acceleration by increasing the value of γ_{max} in successive cells along the emission region. The simulated light curves and spectra are shown in Fig. 7. After fitting the spectra, we obtain the correlations of parameters shown in Fig. 8. α has a weaker anticorrelation with E_{peak} compared to the cooling-dominated case. Multiple values of α are obtained for the same value of E_{peak} and vice versa as shown in Fig. 8 top left panel. That is not commonly seen in the observed results but is indeed found in some epochs, e.g. in Mrk 421 during the 2019 Apr 23 epoch. β has weak correlation or anticorrelation at different intervals, with E_{peak}, similar to the observed results. α and β show anticorrelation at successive intervals denoted by different colours in Fig. 8 bottom left panel. The overall α–β anticorrelation considering the total 5-days time span is weak. This behaviour is similar to the observed results, e.g. bottom right panels of Figs 3 and 4. The flux and peak energy, on the other hand, are uncorrelated, which is different from the observed correlation among those parameters in Mrk 421. In 1ES 1959+650, however, the low-flux states do not exhibit the said correlation between flux and E_{peak}, which matches with the above simulated result. When gradual acceleration is introduced in the theoretical model, the synchrotron peak energy increases with time but the total flux may decrease because electrons lose energy through radiation, the combined effect of which may be responsible for the lack of correlation noted above.

5 SUMMARY AND CONCLUSION

In this paper, we have analysed the X-ray spectra of two HSP blazars Mrk 421 and 1ES 1959+650 at multiple epochs during 2016–2019 at 0.7–20 keV using *AstroSat* and *Swift* data. We have fitted the average spectrum at each epoch with the log-parabola function. We carried out time-resolved spectroscopy with bins of length 10 ks to find the temporal variation of the best-fitting spectral parameters of the log-parabola model. Finally, we compared the results of our analyses to that from two cases of a theoretical model of blazar jet emission, namely, one in which the acceleration time-scale dominates over the radiative cooling time-scale of the highest energy electrons and *vice versa*. In that model, high-energy particles with a simple power-law energy distribution are injected, at a time-scale shorter or longer than the cooling time-scale of the highest energy electrons, in the jet emission region by a moving shock front. The particles cool via radiation through synchrotron and IC processes in the presence of a turbulent magnetic field in the jet. The curvature of the simulated X-ray spectrum is driven by the radiative cooling, while the flux and spectral variability are primarily due to the injection of high-energy particles by the moving front and the fluctuating magnetic field. We find the following:

(1) The time-resolved spectroscopy revealed a strong anticorrelation of the spectral index α with the total flux and peak energy E_{peak}, which indicates a harder-when-brighter trend in the blazars. Furthermore, the correlations of the curvature parameter β with flux and E_{peak} are weak and change sense from one epoch to another, indicating no overall trend while there is an anticorrelation between α and β.

(2) The strong anticorrelation of α and E_{peak}, deduced from the observed spectral variability of Mrk 421 and 1ES 1959+650, match well with the cooling-dominated case of our theoretical model. Similarly, the general harder-when-brighter trend of the X-ray variation is also much better reproduced in the cooling dominated scenario. On the other hand, α and β exhibit a strong anticorrelation in Mrk 421, which is better reproduced in the acceleration dominated case of the model. In one epoch each in Mrk 421 (2019 April 23) and 1ES 1959+650 (2017 October 25) the nature of the α–E_{peak} correlation is different, to a certain extent, from the rest and consequently multiple values of E_{peak} can be found for the same value of α and vice versa (bottom left panels of Figs 3 and 4). That is also found in the simulated results of the acceleration dominated case. Therefore, both cases with gradual acceleration and radiative cooling are partially able to reproduce observational results. This implies that the basic features of the model, i.e. high-energy particles, having a simple power-law energy distribution injected by a shock front moving down the emission region, emitting synchrotron and IC radiation in the presence of a fluctuating magnetic field can give rise to the observed spectral and flux variability properties at hours to days time-scales. However, a model with more complex features in the energy distribution of injected particles, geometric aspects, and emission processes as well as more detailed acceleration mechanisms, e.g. including stochastic acceleration are needed for a better match with all of the observed parameter trends and consequently a more comprehensive interpretation of the observed results.

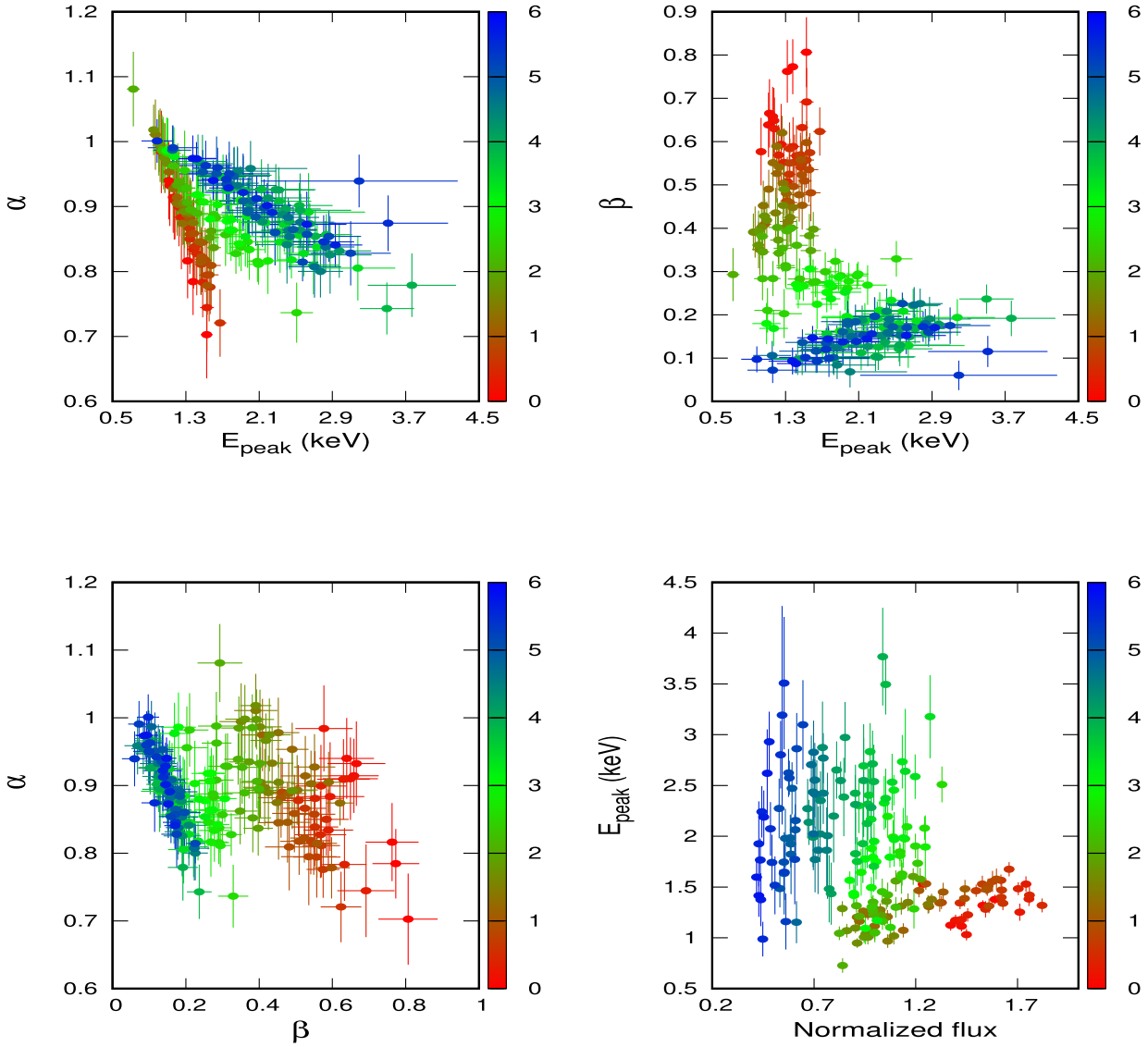

Figure 8. Correlation between the spectral parameters of the log-parabola models, which are best fit to the simulated X-ray spectra at each snapshot of 5 ks duration for the case of gradual acceleration. The colour bar indicates time evolution in days.

(3) Application of a flexible and extensive theoretical model to interpret the comprehensive data set used here makes our inferences fairly robust. It also has the scope of providing more general insight into the blazar phenomena by increasing the number of objects in the sample by a factor of a few and/or extending the parameter space of the theoretical model in a future work.

ACKNOWLEDGEMENTS

We thank the anonymous referee for their comments that have made this work more comprehensive and have provided additional clarity to the presentation. This work has used data from the Indian Space Science Data Centre (ISSDC) under the *AstroSat* mission of the Indian Space Research Organisation (ISRO). We acknowledge the POC teams of the SXT and LAXPC instruments for archiving data and providing the necessary software tools. The data of *Swift*-XRT have been taken from NASA's data repository High Energy Astrophysics Science Archive Research Center (HEASARC). We acknowledge *Swift* team for providing the online software analysis tool. We thank ISRO for support under the *AstroSat* archival data utilization program, **Anusandhan National Research Foundation (ANRF) for a SERB-SURE grant** (SUR/2022/001503), and IUCAA for their hospitality and usage of their facilities during our stay at different times as part of the university associateship program. RC thanks Presidency University for support under the Faculty Research and Professional Development (FRPDF) Grant. We are thankful to Kaustav Mitra and Arit Bala for developing the numerical jet code, which has been used here. We thank Sunil Chandra, Ritesh Ghosh, Savithri Ezhikode, Gulab Dewangan, and Ranjeev Misra for fruitful discussion regarding data analysis for this work.

6 DATA AVAILABILITY

AstroSat data are available in its archival data repository.

Weblink: https://astrobrowse.issdc.gov.in/astro_archive/archive/Home.jsp

The software for data reduction of *AstroSat* are available in *AstroSat Science Support Cell (ASSC)*.

Weblink: http://astrosat-ssc.iucaa.in

The *Swift* data are available in NASA's *HEASARC* archive repository.

Weblink: https://heasarc.gsfc.nasa.gov/

The *Swift*-XRT products are generated by online XRT building product tool.

Weblink: https://www.swift.ac.uk/user_objects/index.php

REFERENCES

Abdo A. A. et al., 2010, ApJ, 716, 30
Abdo A. A. et al., 2011, ApJ, 736, 131
Ackermann M. et al., 2016, ApJ, 824, L20
Albert A. et al., 2022, ApJ, 929, 125
Aliu E. et al., 2013, ApJ, 775, 3
Antia H. M. et al., 2017, ApJS, 231, 10
Banerjee B., Joshi M., Majumdar P., Williamson K. E., Jorstad S. G., Marscher A. P., 2019, MNRAS, 487, 845
Barat S., Chatterjee R., Mitra K., 2022, MNRAS, 515, 1655
Beckmann V., Wolter A., Celotti A., Costamante L., Ghisellini G., Maccacaro T., Tagliaferri G., 2002, A&A, 383, 410
Bhatta G., Mohorian M., Bilinsky I., 2018, A&A, 619, A93
Blandford R. D., Rees M. J., 1978, Phys. Scr, 17, 265
Błażejowski M., Sikora M., Moderski R., Madejski G. M., 2000, ApJ, 545, 107
Bloom S. D., Marscher A. P., 1996, ApJ, 461, 657
Bonning E. et al., 2012, ApJ, 756, 13
Bottacini E., Böttcher M., Pian E., Collmar W., 2016, ApJ, 832, 17
Böttcher M., 2007, Ap&SS, 309, 95
Böttcher M., Dermer C. D., 2010, ApJ, 711, 445
Böttcher M., Reimer A., Sweeney K., Prakash A., 2013, ApJ, 768, 54
Bregman J. N., Lebofsky M. J., Aller M. F., Rieke G. H., Aller H. D., Hodge P. E., Glassgold A. E., Huggins P. J., 1981, Nature, 293, 714
Brinkmann W. et al., 2001, A&A, 365, L162
Brinkmann W., Papadakis I. E., Raeth C., Mimica P., Haberl F., 2005, A&A, 443, 397
Chandra S. et al., 2021, ApJ, 918, 67
Chatterjee R. et al., 2012, ApJ, 749, 191
Chen L., 2014, ApJ, 788, 179
Das S., Chatterjee R., 2023, MNRAS, 524, 3797
Dermer C. D., Schlickeiser R., Mastichiadis A., 1992, A&A, 256, L27
Di Gesu L. et al., 2023, Nat. Astron., 7, 1245
Elvis M., Plummer D., Schachter J., Fabbiano G., 1992, ApJS, 80, 257
Errando M. et al., 2024, ApJ, 963, 5
Evans P. A. et al., 2009, MNRAS, 397, 1177
Fossati G. et al., 2008, ApJ, 677, 906
Ghisellini G., Padovani P., Celotti A., Maraschi L., 1993, ApJ, 407, 65
Ghisellini G., Celotti A., Fossati G., Maraschi L., Comastri A., 1998, MNRAS, 301, 451
Ghisellini G., Righi C., Costamante L., Tavecchio F., 2017, MNRAS, 469, 255
Giebels B. et al., 2002, ApJ, 571, 763
Giommi P. et al., 2012, A&A, 541, A160
Goswami P., Sahayanathan S., Sinha A., Misra R., Gogoi R., 2018, MNRAS, 480, 2046
Goswami P., Sahayanathan S., Sinha A., Gogoi R., 2020, MNRAS, 499, 2094
Graff P. B., Georganopoulos M., Perlman E. S., Kazanas D., 2008, ApJ, 689, 68
Horan D. et al., 2009, ApJ, 695, 596
Hota J., Shah Z., Khatoon R., Misra R., Pradhan A. C., Gogoi R., 2021, MNRAS, 508, 5921
Hu W., Kang J.-L., Cai Z.-Y., Wang J.-X., Su Z.-B., Xiao G.-C., 2024, ApJ, 972, 31
Impey C. D., Neugebauer G., 1988, AJ, 95, 307
Inoue S., Takahara F., 1996, ApJ, 463, 555
Joshi M., Böttcher M., 2011, ApJ, 727, 21
Kalberla P. M. W., Burton W. B., Hartmann D., Arnal E. M., Bajaja E., Morras R., Pöppel W. G. L., 2005, A&A, 440, 775
Kapanadze B., Dorner D., Vercellone S., Romano P., Kapanadze S., Mdzinarishvili T., 2016, MNRAS, 461, L26
Kapanadze B., Dorner D., Romano P., Vercellone S., Kapanadze S., Tabagari L., 2017, ApJ, 848, 103
Kapanadze B. et al., 2018, ApJS, 238, 13
Kapanadze B. et al., 2020, ApJS, 247, 27
Khatoon R., Shah Z., Hota J., Misra R., Gogoi R., Pradhan A. C., 2022, MNRAS, 515, 3749
Kim D. E. et al., 2024, A&A, 681, A12
Konigl A., 1981, ApJ, 243, 700
Kouch P. M. et al., 2024, A&A, 689, A119
Kundu A., Chatterjee R., Mitra K., Mondal S., 2022, MNRAS, 510, 3688
Landau R. et al., 1986, ApJ, 308, 78
Lichti G. G. et al., 2008, A&A, 486, 721
Lin Y. C. et al., 1992, ApJ, 401, L61
Liodakis I. et al., 2022, Nature, 611, 677
Liu R.-Y., Xue R., Wang Z.-R., Tan H.-B., Böttcher M., 2023, MNRAS, 526, 5054
MAGIC Collaboration, 2020, A&A, 638, A14
Maraschi L., Ghisellini G., Celotti A., 1992, ApJ, 397, L5
Markowitz A. G. et al., 2022, MNRAS, 513, 1662
Marscher A. P., 1998, in Zensus J. A., Taylor G. B., Wrobel J. M.eds, ASP Conf. Ser. Vol. 144, IAU Colloq. 164: Radio Emission from Galactic and Extragalactic Compact Sources. Astron. Soc. Pac., San Francisco, p. 25
Marscher A. P., 2014, ApJ, 780, 87
Marscher A., 2016, Galaxies, 4, 37
Marscher A. P., Di Gesu L., Jorstad S. G., Kim D. E., Liodakis I., Middei R., Tavecchio F., 2024, Galaxies, 12, 50
Massaro F., Tramacere A., Cavaliere A., Perri M., Giommi P., 2008, A&A, 478, 395
Massaro E., Perri M., Giommi P., Nesci R., 2004, A&A, 413, 489
Massaro E., Tramacere A., Perri M., Giommi P., Tosti G., 2006, A&A, 448, 861
Massaro F., Paggi A., Cavaliere A., 2011, ApJ, 742, L32
Massaro F., Thompson D. J., Ferrara E. C., 2015, A&AR, 24, 2
Mastichiadis A., Kirk J. G., 1997, A&A, 320, 19
Middei R. et al., 2023, ApJ, 953, L28
Mücke A., Protheroe R. J., 2001, Astropart. Phys., 15, 121
Mücke A., Protheroe R. J., Engel R., Rachen J. P., Stanev T., 2003, Astropart. Phys., 18, 593
Nishiyama T., 1999, in Kieda D., Salamon M., Dingus B., eds, Proceedings of the 26th International Cosmic Ray Conference. August 17-25, 1999. Salt Lake City, Utah, USA. Under the auspices of the International Union of Pure and Applied Physics (IUPAP). Volume 3. p. 370
Peirson A. L., Romani R. W., 2018, ApJ, 864, 140
Peirson A. L., Romani R. W., 2019, ApJ, 885, 76
Piner B. G., Unwin S. C., Wehrle A. E., Edwards P. G., Fey A. L., Kingham K. A., 1999, New Astron. Rev., 43, 711
Punch M. et al., 1992, Nature, 358, 477
Rajput B., Stalin C. S., Rakshit S., 2020, A&A, 634, A80
Sambruna R. M., Maraschi L., Urry C. M., 1996, ApJ, 463, 444
Shah Z., Ezhikode S. H., Misra R., Rajalakshmi T. R., 2021, MNRAS, 504, 5485
Sikora M., Begelman M. C., Rees M. J., 1994, ApJ, 421, 153
Singh K. P. et al., 2014, in Takahashi T., den Herder J.-W. A., Bautz M.eds, Proc. SPIE Conf. Ser. Vol. 9144, Space Telescopes and Instrumentation 2014: Ultraviolet to Gamma Ray. SPIE, Bellingham, p. 91441S
Singh K. P. et al., 2016, in den Herder J.-W. A., Takahashi T., Bautz M., eds, Proc. SPIE Conf. Ser. Vol. 9905, Space Telescopes and Instrumentation 2016: Ultraviolet to Gamma Ray. SPIE, Bellingham, p. 99051E
Singh K. P. et al., 2017, JA&A, 38, 29
Sironi L., Spitkovsky A., 2014, ApJ, 783, L21
Tagliaferri G., Ravasio M., Ghisellini G., Tavecchio F., Giommi P., Massaro E., Nesci R., Tosti G., 2003, A&A, 412, 711

Takahashi T. et al., 1996, ApJ, 470, L89
Tanihata C., Kataoka J., Takahashi T., Madejski G. M., 2004, ApJ, 601, 759
Tavecchio F., 2021, Galaxies, 9, 37
Tramacere A., Massaro F., Cavaliere A., 2007, A&A, 466, 521
Tramacere A., Giommi P., Perri M., Verrecchia F., Tosti G., 2009, A&A, 501, 879
Urry C. M., Mushotzky R. F., 1982, ApJ, 253, 38
Urry C. M., Padovani P., 1995, PASP, 107, 803
Wani K., Gaur H., Patil M. K., 2023, ApJ, 951, 94
Weisskopf M. C. et al., 2022, J. Astron. Telesc. Instrum. Syst., 8, 026002
Yadav J. S. et al., 2016, in den Herder J.-W. A., Takahashi T., Bautz M.eds, Proc. SPIE Conf. Ser. Vol. 9905, Space Telescopes and Instrumentation 2016: Ultraviolet to Gamma Ray. SPIE, Bellingham, p. 99051D

APPENDIX A: SPECTRAL MODELLING

The log-parabola model in terms of photon flux can be expressed as

$$F(E) = N_0(E/E_0)^{-\alpha-\beta log_{10}(E/E_0)}\,, \tag{A1}$$

where N_0 is a normalization factor, E_0 is pivot energy, and α and β are the photon index and curvature around the peak of the function, respectively. Using those parameters, the peak energy and height of the peak are calculated by $E_p = E_0 10^{(2-\alpha)/2\beta}$ keV and $S_p = E_p^2 F(E_p)$ erg cm^{-2} s^{-1} (Massaro et al. 2008).

The average spectra are fitted by the above model for all epochs of Mrk 421 and 1ES 1959+650. The best-fitting models are shown in Figs A1 and A2.

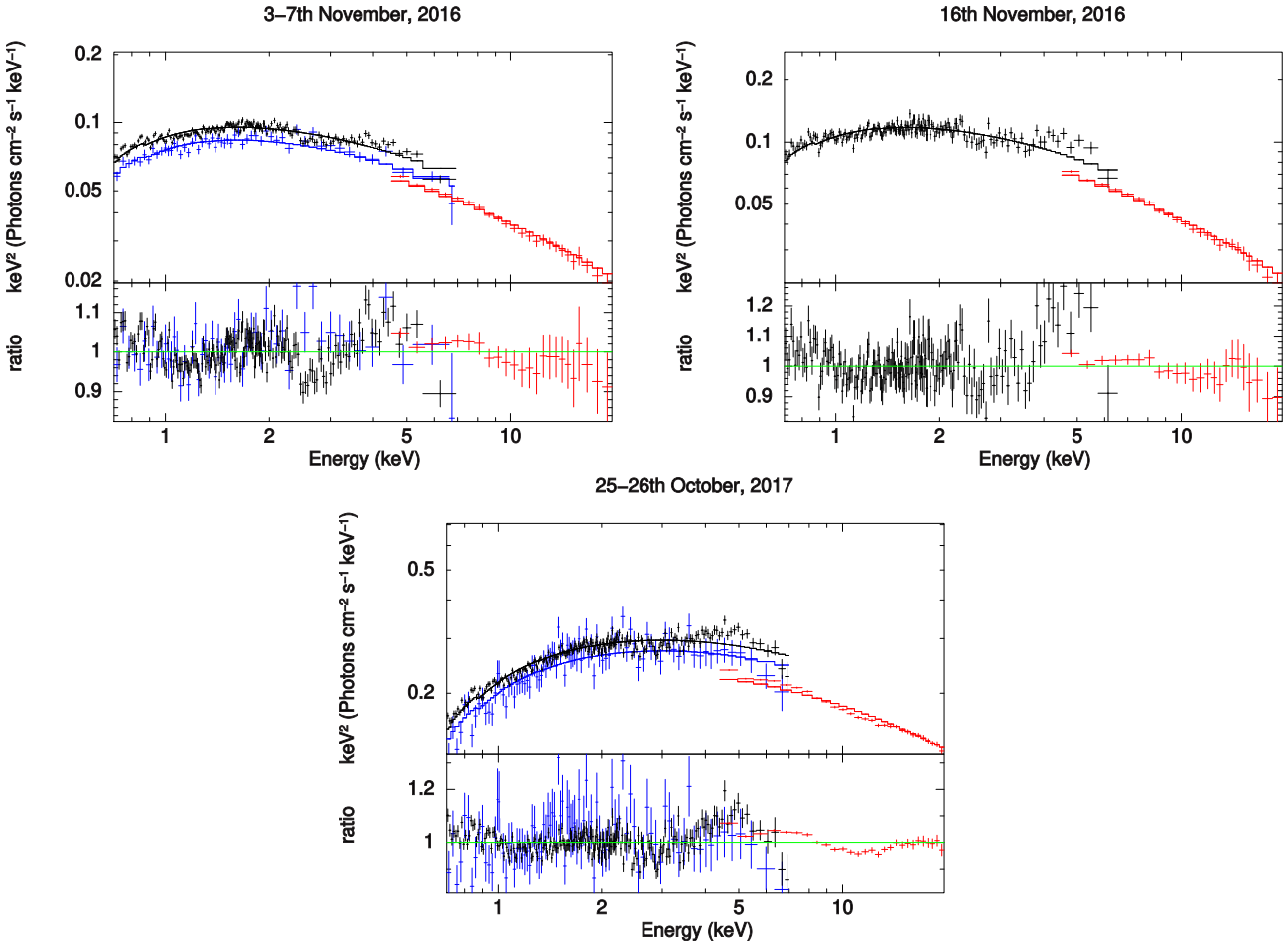

Figure A1. XRT (blue), SXT (black), and LAXPC (red) data points and the best-fitting log-parabola model (solid lines) of the combined unfolded spectra of the blazar 1ES 1959+650 during three epochs in 2016–2017.

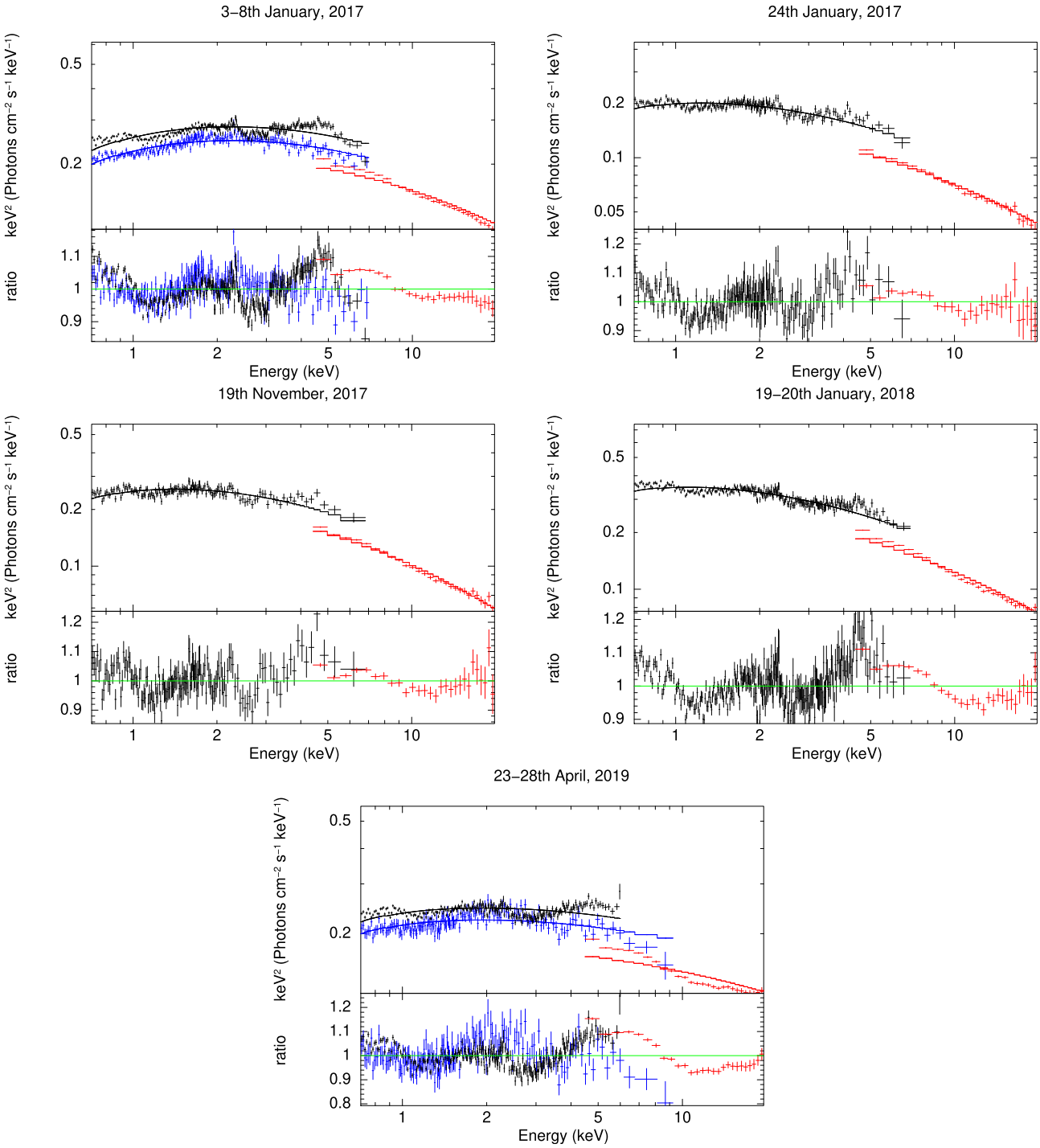

Figure A2. XRT (blue), SXT (black), and LAXPC (red) data points and the best-fitting log-parabola model (solid lines) of the combined unfolded spectra of the blazar Mrk 421 during five epochs in 2017–2019.

This paper has been typeset from a TEX/LATEX file prepared by the author.